ACS APPLIED MATERIALS & INTERFACES

Research Article

www.acsami.org

Supersaturation-Controlled Shape Evolution of α-Fe_2O_3 Nanocrystals and Their Facet-Dependent Catalytic and Sensing Properties

Junjie Ouyang, Jun Pei, Qin Kuang,* Zhaoxiong Xie,* and Lansun Zheng

State Key Laboratory of Physical Chemistry of Solid Surfaces and Department of Chemistry, College of Chemistry and Chemical Engineering, Xiamen University, Xiamen 361005, China

Supporting Information

ABSTRACT: Surface engineering of crystals at nanoscale level by precisely and rationally exposing specific facets proved to be highly effective in enhancing the performance of inorganic functional nanocrystals. To do so, a comprehensive understanding of the growth mechanism was of great importance. By using hematite (α-Fe_2O_3) as an example, in this paper we demonstrated high effectiveness of controlling supersaturation of growth monomers in engineering the exposed facets of nanocrystals. Under surfactant-free hydrothermal conditions, a series of morphology evolution of α-Fe_2O_3 nanocrystals from {012} faceted pseudocubes to {113} faceted hexagonal bipyramids and {001} faceted nanoplates were successfully activated through concentration-, reaction time-, and solvent-dependent hydrolysis of ferric acetylacetonate. High supersaturation was eventually proven to be conducive to the formation of facets with high surface energy. Furthermore, the α-Fe_2O_3 nanocrystals enclosed with facets of high surface energy exhibited excellent catalytic activity and gas-sensing ability. The present work will deepen our understanding of thermodynamics and kinetic control over the morphology of nanocrystals as well as our understanding of surface-related performance of inorganic functional nanocrystals.

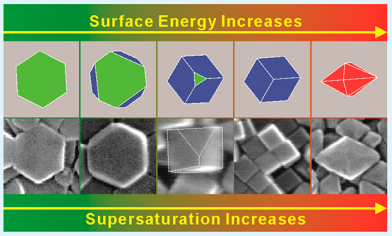

KEYWORDS: *Supersaturation, Hematite, Shape evolution, CO catalysis, Gas sensing*

1. INTRODUCTION

The precise fabrication of crystals with specific shape at nanoscale level is crucial for enhancing their performance in many applications, such as catalysis, gas sensing, solar conversion, and so on.[1−4] Such shape effect inherently results from the atomic arrangement on different exposed crystal facets. To achieve control over the growth behavior of nanocrystals, it is necessary to understand the thermodynamic and kinetic mechanisms by which nanocrystals form.[5] In the past decade, the structure-directing effect of some specific inorganic ions or organic macromolecules on the shape of nanocrystals has been intensively investigated.[6−9] It is well-accepted that these agents can thermodynamically alter the relative free energies of different crystal faces and their growth rates by means of specific adsorption. In fact, supersaturation of growth monomers in reaction solution is a key factor that was often missed in the study of shape control of nanocrystals, since it is always involved in too many experimental parameters, including concentration, reaction time, temperature, solvent, and so on. The term "growth monomers," also known as "growth units," is solute (crystal building block) in crystal growth solutions. Recently, a great deal of studies have revealed that whether nanomaterials are ionic, molecular, or metallic crystals, the surface can still be easily controlled via adjusting supersaturation of growth monomers during the growth process.[8−15] However, a comprehensive understanding of supersaturation on the crystal shape is susceptible to the interference from the use of additives, especially those facet-capping agents.[8,9] Therefore, it is a great challenge to recognize the influence of supersaturation on the surface structure during the growth of nanocrystals in complicated environmental conditions.

Among metal oxides, ferric oxide (Fe_2O_3) is known as its varied polymorphs.[16−18] Hematite (i.e., α-Fe_2O_3) with a corundum-type structure ($R\bar{3}c$ space group, a = 0.50352 and c = 1.37508 nm) is thermodynamically the most stable phase of ferric oxide under ambient conditions.[16] As an important n-type semiconductor (E_g = 2.1 eV), α-Fe_2O_3 has been extensively used as gas-sensing materials, catalysts, absorbents for heavy metal ion removal, and electrode materials for photovoltaic and photoelectrochemical devices, due to its low cost, nontoxicity, high resistance to corrosion, and strong visible light absorption.[19−26] Recently, increasing attention has been paid to rationally engineering surface structures of α-Fe_2O_3 nanocrystals, whereby the performance in surface-related applications were significantly enhanced.[27−33] Up to now, various α-Fe_2O_3 nanocrystals enclosed by specific facets, such as {113} faceted hexagonal bipyramid-like dodecahedra, {012} faceted pseudocubes (actually rhombohedra that look like cubes), and {104} faceted rhombohedra, have been successfully fabricated via various wet chemical routes on the basis of hydrolysis of Fe(III) ions.[27,28,34−38] In the reported approaches, foreign inorganic or organic additives as capping agents are mostly necessary to tune the growth behavior of α-Fe_2O_3

Received: April 22, 2014
Accepted: July 8, 2014
Published: July 8, 2014

Table 1. Summary of Synthetic Parameters for the Three Kinds of α-Fe_2O_3 Nanocrystals

sample	$Fe(acac)_3$ (mmol)	NaOH (mmol)	OA (mL)	ethanol (mL)	water (mL)	stirring treatment
bipyramid-Fe_2O_3-{113}	1.0	3.0	5.0	5.0	5.0	not applied
pseudocube-Fe_2O_3-{012}	1.0	3.0	5.0	5.0	5.0	applied
plate-Fe_2O_3-{001}/{012}	1.0	3.0	5.0	10.0	0.3	applied

nanocrystals. Interestingly, these capping reagents sometimes have no essential effect on the shape of the formed α-Fe_2O_3 nanocrystals. For example, {104} faceted rhombohedral nanocrystals can be formed in both additive-free and formamide (or PVP)-assisted ferric chloride solutions.[27,28,34,35] At the same time, it has been revealed in some studies that the concentration of the ferric precursor plays a decisive role in the morphology evolution from pseudocubes to truncated bipyramid-like tetrakadecahedra, whereas the amount of additives merely tunes the aspect ratio of exposed facets.[31] Given that, the morphology of α-Fe_2O_3 nanocrystals, that is, the exposed facets, might be correlated with the supersaturation of the reaction system.

In this paper, by using α-Fe_2O_3 nanocrystals as an example, we fully demonstrate the high effectiveness of supersaturation control over the morphology of nanocrystals during crystal growth. We successfully fabricated α-Fe_2O_3 nanocrystals exposed with three kinds of crystal facets, including {113} faceted hexagonal bipyramids, {012} faceted pseudocubes, and {001} faceted nanoplates, based on the hydrolysis of ferric acetylacetonate under surfactant-free hydrothermal conditions. Given the absence of surfactants, the influence of supersaturation on the surface structure of α-Fe_2O_3 nanocrystals can be definitively identified through various condition-controlled synthetic experiments where the concentration of the precursors, reaction time, and solvent components were in particular investigated. Furthermore, we investigated the catalytic performances of three α-Fe_2O_3 nanocrystals in CO oxidation and their gas-sensing ability, since the success in facet control offers a unique opportunity to deeply understand the nature of the structure–performance relationship of nanocrystals.

2. EXPERIMENTAL SECTION

2.1. Materials. Iron(III) 2,4-pentanedionate ($Fe(acac)_3$) and oleic acid (OA, 90%) were purchased from Alfa Aesar, and sodium hydroxide (NaOH, 96%) was purchased from Guangdong Guanghua Sci-Tech Co., Ltd. All chemicals were used as received without further purification. Deionized water was used throughout experiments.

2.2. Syntheses of α-Fe_2O_3 Nanocrystals with Morphologies of Hexagonal Bipyramid, Pseudocube, and Hexagonal Plate. Three kinds of polyhedral α-Fe_2O_3 nanocrystals were prepared via a facile hydrothermal route. In a typical synthetic process of hexagonal bipyramidal α-Fe_2O_3 nanocrystals enclosed by {113} facets, $Fe(acac)_3$ (1 mmol, 0.3531 g) and a NaOH aqueous solution (0.6 M, 5 mL) were successively added into a mixed solvent of OA (5 mL), ethanol (5 mL), and water (5 mL) without any stirring. The resulting mixture was transferred to a Teflon-lined stainless steel autoclave (25 mL) and kept at 180 °C for 24 h. The products were collected by centrifugation at 8000 rpm for 3 min, washed several times with hexane, and dried at room temperature. For further characterization, the sample was put in a furnace and heated at 250 °C for 15 min to remove the organic residues. For hexagonal bipyramidal α-Fe_2O_3 nanocrystals, an alternative synthetic method was applied by increasing the amount of $Fe(acac)_3$ from 1 to 2 mmol under vigorous stirring, with the other synthetic procedures and conditions unchanged.

The morphology evolution of α-Fe_2O_3 nanocrystals was achieved by controlling the supersaturation of reaction solution with tuning the concentrations of Fe source, the reaction time, and/or the composition of solvent. For synthesizing the pseudocubic α-Fe_2O_3 nanocrystals enclosed by {012} facets, vigorous stirring was introduced into the same synthetic procedure with bipyramidal α-Fe_2O_3 nanocrystals using 1 mmol $Fe(acac)_3$ as source, whereby fully homogeneous reaction solution were formed. And for preparing hexagonal platelike α-Fe_2O_3 nanocrystals enclosed by {001}/{012} facets, $Fe(acac)_3$ (1 mmol, 0.3531 g) and NaOH ethanol solution (0.6 M, 5 mL) was successively added into the mixture of OA (5 mL), ethanol (5 mL), and H_2O (0.3 mL) under intense ultrasonic condition, followed by vigorous stirring. Besides that, other synthetic procedures and conditions remained the same with the synthesis of hexagonal bipyramidal α-Fe_2O_3 nanocrystals. The detailed synthetic parameters are listed in Table 1 and, in the Supporting Information, Tables S1–S3.

2.3. Characterization of Samples. The compositions of the as-prepared samples were determined by powder X-ray diffraction (XRD) patterns recorded on a Rigaku Ultima IV X-ray diffractometer with Cu Kα radiation. The morphology and structure of the as-prepared samples were observed by using scanning electron microscope (SEM, Hitachi S4800) and transmission electron microscope (TEM, JEOL JEM 2100) with an acceleration voltage of 200 kV. All TEM samples were prepared by depositing a drop of diluted suspension in distilled ethanol on a copper grid coated with carbon film. The specific surface areas of the samples were determined by measuring nitrogen adsorption and desorption isotherms on a Micrometrics ASAP 2020 system according to the Brunauer–Emmett–Teller (BET) method. The dispersions of surface-active sites of the samples were determined by CO chemisorption measurements on a Micrometrics ASAP 2020 system. The surface compositions of the samples were determined by a Qtac-100 LEISS-XPS system. The binding energies were calibrated with respect to the signal for adventitious carbon (binding energy of 284.7 eV).

2.4. CO Catalytic Oxidation Measurements of Samples. The catalytic activity measurements of the pristine α-Fe_2O_3 nanocrystals toward CO oxidation were carried out in a quartz tubular fixed-bed reactor in the temperature range from room temperature to 400 °C. For each test, about 100 mg of Fe_2O_3 samples, which was normalized by using their BET surface areas, was placed at the center of the reactor using quartz glass wool as plugs. The reaction gas, which was mixed with 5% CO in nitrogen (10 mL·min^{-1}) and air (40 mL·min^{-1}), was fed to the reactor. The outlet gas was analyzed online by using an on-stream gas chromatograph (FuLi 9790II) equipped with a TDX-01 column after the catalyst bed temperature was stabilized at a settled value for 10 min to obtain the steady state.

2.5. Gas-Sensing Measurements of Samples. The gas-sensing measurements of the as-prepared Fe_2O_3 samples were carried out on a WS-30A sensor measurement system (Zhengzhou Winsen Electronics Technology, China).[39] In a typical test, a gas sensor was fabricated by coating a certain amount of Fe_2O_3 paste (consisting of Fe_2O_3 nanoparticles and the ethanol solvent) onto a ceramic tube that was previously mounted with Au electrodes and Pt conducting wires. An alloy filament was inserted through the tube as a heater to provide the operation temperature from 200 to 500 °C. Before testing, the sensor was aged in air for 24 h at 300 °C to achieve the device stabilization. After that, a certain volume of liquid analytes (e.g., acetone and methanol) was injected with a microsyringe onto a metal-plate heater in the test chamber, and the concentration of the evaporated gas was calculated according to the total volume (27 L) of gas chamber. Here the gas-sensing ability (S) of the sensor was defined as the ratio R_{air}/R_{gas}, where R_{air} and R_{gas} are the electrical resistance of the sensor in air and in the test gas at the operation temperature, respectively. For

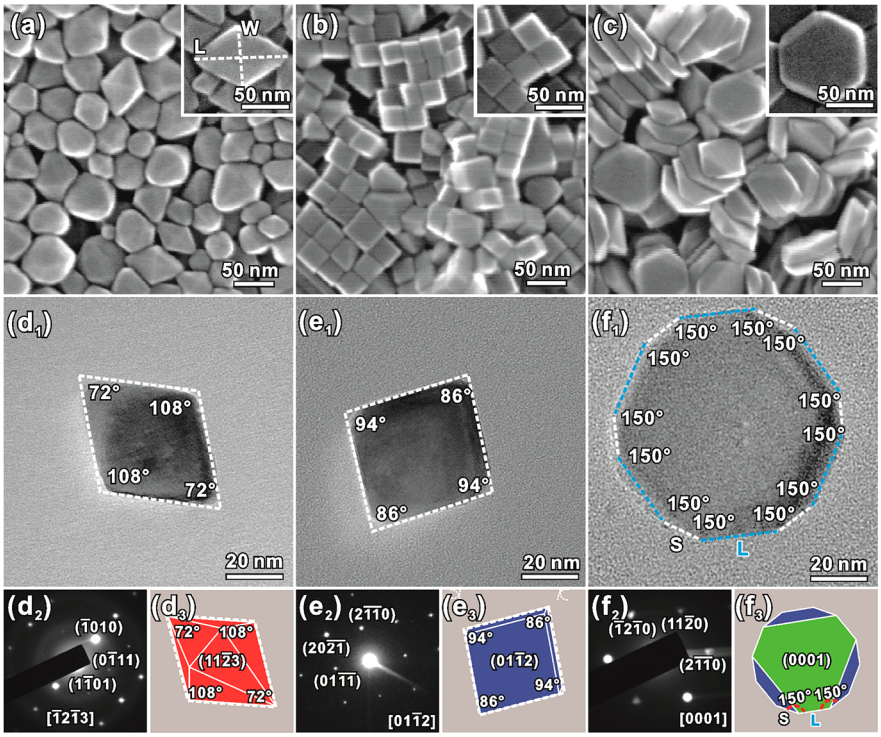

Figure 1. (a–c) SEM images of the as-prepared bipyramid-Fe_2O_3-{113}, pseudocube-Fe_2O_3-{012}, and plate-Fe_2O_3-{001}/{012} nanocrystals. (insets) High-magnification SEM images. (d_1–f_1) TEM images, (d_2–f_2) SAED patters, and (d_3–f_3) corresponding ideal geometrical models of individual α-Fe_2O_3 nanocrystals with three kinds of morphologies. In the ideal geometrical models, the {113}, {012}, and {001} facets are presented in red, blue, and green, respectively.

comparison, all sensors were fabricated with the same amount of nanocrystals.

3.1. RESULTS AND DISCUSSION

3.1. Structure and Morphology of Three Kinds of α-Fe_2O_3 Nanocrystals. Figure 1a–c shows typical low-magnification SEM images of the three as-prepared α-Fe_2O_3 nanocrystals, indicating high purity in their morphology. As shown in Figure 1a, the α-Fe_2O_3 nanocrystals synthesized without stirring treatment on reaction solution, consisting of $Fe(acac)_3$ (1 mmol), NaOH (0.6 M, 5 mL), OA (5 mL), and ethanol (5 mL), are well-shaped hexagonal bipyramids. The edge-to-edge widths (W) of bipyramids are 25–50 nm, and the apex-to-apex lengths (L) are 50–100 nm. Further TEM observation and selected-area electron diffraction (SAED) (Figure 1d_1,d_2) indicates that the single hexagonal bipyramidal α-Fe_2O_3 nanocrystal displays a diamond projection profile with angles of 72° and 108° under electron beam along the [$\bar{1}2\bar{1}3$] (i.e., [$\bar{1}23$] in three-index notation) zone axis of rhombohedral α-Fe_2O_3. Note that these angles agree well with the model of an ideal hexagonal bipyramidal α-Fe_2O_3 nanocrystal enclosed by {113} facets projected along the [$\bar{1}2\bar{1}3$] zone axis (Figure 1d_3).

Typical morphology of the pseudocubic α-Fe_2O_3 nanocrystals synthesized with stirring treatment on the same reaction solution consisting of 1 mmol of $Fe(acac)_3$ is presented in Figure 2b. The pseudocubic α-Fe_2O_3 nanocrystals are relatively uniform in size, and the mean size is ca. 30 nm. The high-magnification SEM image and TEM observation indicate that these pseudocubic nanocrystals actually have an oblique parallelepiped morphology, which consists of six identical parallelogram facets. The dihedral angles between two adjacent facets are 86° or 94° (Figure 1b,e_1). In fact, an ideal

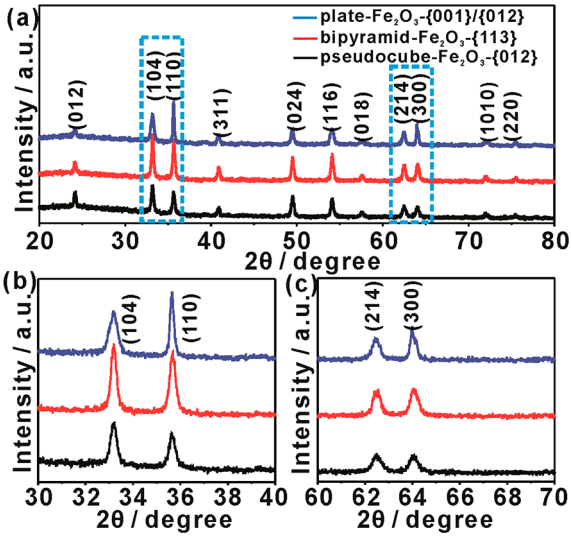

Figure 2. (a) XRD patterns of the as-prepared bipyramid-Fe_2O_3-{113}, pseudocube-Fe_2O_3-{012}, and plate-Fe_2O_3-{001}/{012} nanocrystals. (b–c) Enlarged region around the (104)/(110) and (214)/(300) diffraction peaks of the three samples.

rhombohedron enclosed by {012}, due to the appropriate c/a ratio of the rhombohedral unit cell of α-Fe_2O_3, resembles a cube and thus is commonly referred to as pseudocube or quasicube. The structural features of the as-prepared pseudocubic nanocrystals is apparently in good agreement with the geometrical model of an ideal rhombohedron enclosed by {012} facets when projected along the same zone axis of [01$\bar{1}$2] (i.e., [012] in three-index notation) (Figure 1e_3).

dx.doi.org/10.1021/am502358g | ACS Appl. Mater. Interfaces 2014, 6, 12505–12514

Figure 1c shows typical morphology of the Fe_2O_3 nanocrystals synthesized with changing the ratio of water to ethanol in mixed solvent from 1:1 to 3:100. The as-prepared product is composed of two-dimensional platelike nanocrystals, which are ca. 100 nm in size and ca. 18 nm in thickness. The top-view SEM image (inset of Figure 1c) reveals that the as-prepared Fe_2O_3 nanoplates seem hexagonal. Interestingly, vertically aligned nanoplates are frequently seen in SEM observation, which clearly indicates that the sides of these nanoplates are not perpendicular to the bottom/top surface but are alternately wedge-shaped. A similar morphology feature was found in the previously reported Fe_2O_3 nanoplates, which are proven to be enclosed by two {001} top/bottom and six {012} sides.[40] Through careful survey, it was found that the nanoplates when lying display a truncated hexagonal profile where there are six long edges (L) and six short edges (S), and the angle between the long edge and the short edge is equal to 150°, as marked in Figure 1f$_1$. The corresponding SAED pattern (Figure 1f$_2$) presents a set of diffraction spots with hexagonal symmetry, which can be indexed as the [0001] zone axis of rhombohedral α-Fe_2O_3. This indicates that the nanoplates are single crystalline and the bottom/top surface are indeed bounded by {001}. The above structural features agree with the model of an ideal α-Fe_2O_3 nanoplate enclosed by six {012} facets and two {001} facets projected along the [0001] zone axis (Figure 1f$_3$).

On the basis of the above structural analysis, it can be concluded that the hexagonal bipyramidal, and pseudocubic α-Fe_2O_3 nanocrystals are enclosed with twelve {113} facets and six {012} facets, respectively, while the platelike α-Fe_2O_3 nanocrystals are enclosed by two {001} facets as the bottom/top surface and six {012} facets as the side surface. For convenience, the three kinds of polyhedral α-Fe_2O_3 nanocrystals above are denoted as the form "morphology-Fe_2O_3-{facets}", that is, bipyramid-Fe_2O_3-{113}, pseudocube-Fe_2O_3-{012}, and plate-Fe_2O_3-{001}/{012}, respectively.

The α-Fe_2O_3 phase of three products was proven by the corresponding XRD patterns. As shown in Figure 2a, all diffraction peaks of the three samples can be well-indexed to the rhombohedral α-Fe_2O_3 with cell constants of a = 5.0356 Å and c = 13.7489 Å (JCPDS No. 33−0664). No impurity peaks are observed, and the diffraction peaks are comparatively sharp, suggesting that the as-synthesized α-Fe_2O_3 nanocrystals have good crystallinity. Note that the width and relative intensity of some specific diffraction peaks of the platelike Fe_2O_3 sample are obviously different, in comparison with the other two samples. Typically, the (110) and (300) ({hk0}) diffraction peaks of the plate-Fe_2O_3-{001}/{012} nanocrystals display narrower width compared to the (104) and (214) ({hkl}) diffraction peaks, as shown in Figure 2b,c. Accompanied with the peak narrowing, the {hk0} diffraction peaks of the plate-Fe_2O_3-{001}/{012} nanocrystals become abnormally higher, which is consistent with the XRD pattern of Fe_2O_3 nanoplates in previous reports.[40] These results mean that the α-Fe_2O_3 nanocrystals have better crystal development in the a- than in the c-direction, agreeing with the two-dimensional nature of the platelike nanocrystals. The morphology of nanocrystals grown in specific conditions is known to depend on the growth rates of different facets. The appearance of the platelike α-Fe_2O_3 nanocrystals revealed that the vertical growth of α-Fe_2O_3 along c-axis is confined, but the radial one along a,b-axis is enhanced.[40]

3.2. Supersaturation-Controlled Shape Evolution of α-Fe_2O_3 Nanocrystals. In the classic crystal growth theory, the formation of a crystal can be divided into two separate stages, namely, nucleation and growth, and in both stages supersaturation is the primary driving force. The effect of supersaturation on the size of nanocrystals, that is, high supersaturation easily leads to a short nucleation burst and the production of a large number of a very small crystallites, has been well-accepted to date.[41] This phenomenon was well-explained by the Thomson−Gibbs equation ($\Delta\mu = \mu_1 - \mu_c = 2\sigma\upsilon/h$) (see Supporting Information for detailed description), which was originated from thermodynamics equilibrium.[42] Deduced from the Thomson−Gibbs equation, we recently proposed that during the crystal growth process, the excessive energy for transforming the solute into crystal should be transferred to surface energy of crystallites.[13] Since the surface energy of crystal face is in proportion to the supersaturation of crystal growth monomers during the crystal growth, the exposed faces of nanocrystal can be tuned by simply controlling the supersaturation.

Note that the supersaturation of growth monomers is associated with many synthetic parameters, for example, concentration, reaction time and temperature, composition of solvents, stirring, etc. Changing one of these synthetic parameters will change the supersaturation of the system, leading to a morphology evolution of as-formed nanocrystals. Typically, in our synthetic processes of the bipyramid-Fe_2O_3-{113} and pseudocube-Fe_2O_3-{012} samples, all other operations and conditions were kept the same, except for stirring treatment of the reaction solution (see the Experimental Section for details). Without stirring treatment, the hexagonal bipyramidal α-Fe_2O_3 nanocrystals exposed with {113} facets were produced. But with stirring treatment, the produced α-Fe_2O_3 nanocrystals became pseudocubes exposed with {012} facets. This is a very interesting phenomenon. As we know, $Fe(acac)_3$ has a relatively low solubility in water−ethanol solution, and thus stirring treatment is normally required to accelerate the dissolution of $Fe(acac)_3$ and to evenly distribute Fe^{3+} in the solution. Without stirring, $Fe(acac)_3$ dissolves slowly, thereby producing a local high concentration of Fe^{3+} at the bottom of the reaction solution. From the above analysis, it is easily deduced that higher concentrations are more conducive to the formation of the bipyramid-Fe_2O_3-{113} nanocrystals if reaction solutions are fully homogeneous by stirring.

This conjecture was supported strongly by our results in concentration-dependent experiments (see Supporting Information, Table S1 for detailed reaction parameters). As shown in Figure 3, the morphology of α-Fe_2O_3 nanocrystals was successfully controlled by changing the amount of $Fe(acac)_3$ added to the reaction. When 1 mmol of $Fe(acac)_3$ was added under stirring, pseudocubic Fe_2O_3 nanocrystals were obtained (Figure 3a). But when the amount of $Fe(acac)_3$ increased to 2 mmol under stirring, hexagonal bipyramidal Fe_2O_3 nanocrystals exposed with {113} facets were obtained as predicted (Figure 3b). This result indicates that the formation of Fe_2O_3 nanocrystals exposed with {113} facets is really favored in the relatively high concentration of Fe^{3+} source. Noticeably, the exposed facets became more uncertain when the Fe^{3+} concentration was further increased. For example, more and more nearly spherical nanocrystals, which are bounded by multiple groups of uncertain high-index facets, were produced as the amount of $Fe(acac)_3$ was increased to 3 mmol (Figure 3c) and further to 4 mmol (Figure 3d). Previous calculation studies have revealed that the average surface energy of α-

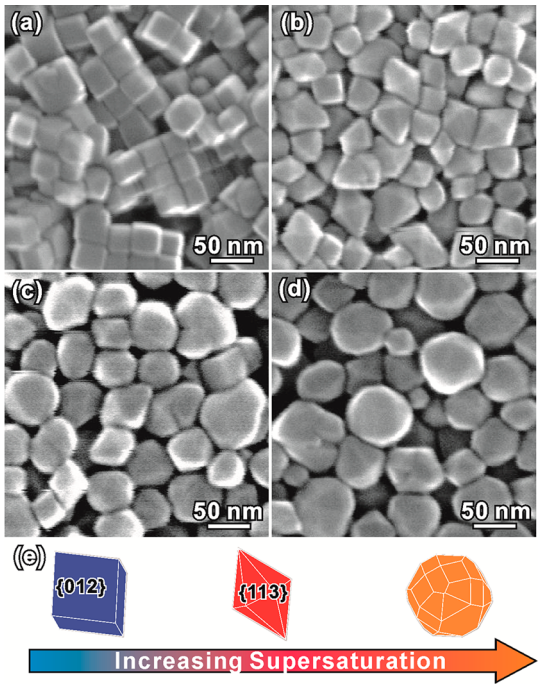

Figure 3. SEM images of α-Fe_2O_3 nanocrystals synthesized with different amounts of $Fe(acac)_3$: (a) 1 mmol; (b) 2 mmol; (c) 3 mmol; (d) 4 mmol. (e) Schematic illustration of the supersaturation-controlled morphology evolution of α-Fe_2O_3 nanocrystals, which was activated by changing concentrations of Fe^{3+} source.

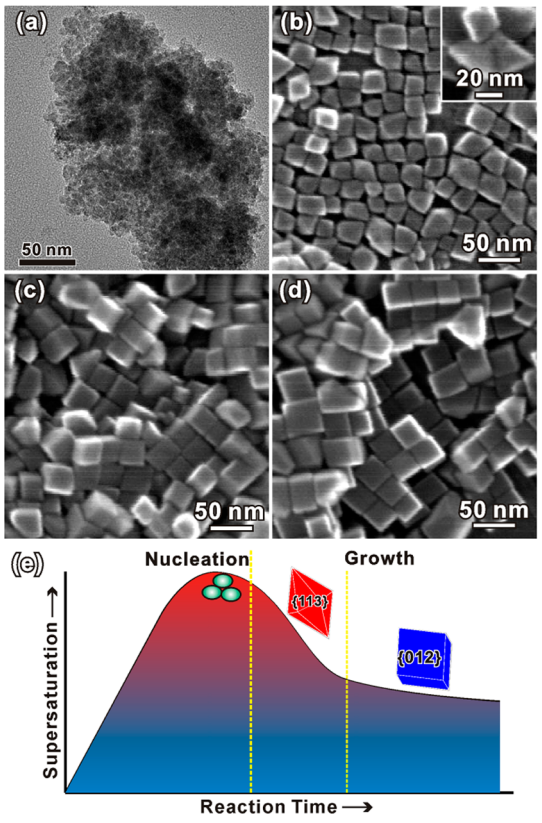

Figure 4. SEM (or TEM) images of α-Fe_2O_3 nanocrystals synthesized at 180 °C for different times: (a) 1 h; (b) 3 h; (c) 6 h; (d) 9 h. (e) Schematic illustration of the supersaturation-controlled morphology evolution of α-Fe_2O_3 nanocrystals as a function of reaction time.

Fe_2O_3 is {012} < {113} and the crystal growth rate of α-Fe_2O_3 is accordingly {012} < {113}.[43,44] In the present study, the bipyramid-Fe_2O_3-{113} nanocrystals with higher surface energy were favored in higher concentration of $Fe(acac)_3$ (2 mmol), which created a higher supersaturation for the Fe_2O_3 crystal growth (Figure 3e). Therefore, this result is consistent with the proposed supersaturation-controlled morphology evolution rule.

As we know, the supersaturation of growth monomers largely depends on the original concentrations of precursors and changes as the reaction proceeds. Such a supersaturation change leads to great evolution of the nanocrystal morphology as reaction time increases. To prove this, time-dependent reaction experiments were further carried out. Figure 4 shows typical morphology of the products obtained by using 1 mmol of $Fe(acac)_3$ as source for reaction duration of 1, 3, 6, and 9 h (see Supporting Information, Table S2 for detailed conditions). After reaction for 1 h, a large amount of premature crystallites of 5 nm in size were observed in reaction solution, indicating that the Fe_2O_3 crystal nucleus began to form as the reaction progressed (Figure 4a and Supporting Information, Figure S1a). When the reaction lasted for 2 h, some bipyramidal nanocrystals began to form, and their sizes were in the range of 20−30 nm (see Supporting Information, Figure S1b). When the reaction time was extended to 3 h, well-defined hexagonal bipyramidal nanocrystals exposed with {113} facets had grown up (Figure 4b). These bipyramidal nanocrystals, which have the edge-to-edge width of 25−40 nm and the apex-to-apex length of 40−50 nm, are much smaller than the matured bipyramidal nanocrystals shown in Figure 1a. After 6 h, the products completely evolved into the pseudocubic α-Fe_2O_3 nanocrystals exposed with {012} facets (Figure 4c). Even if the reaction time was further extended to 9 h, the pseudocubic α-Fe_2O_3 nanocrystals still dominated in the products (Figure 4d). This result means {012} facets are thermodynamically more stable and therefore grow slower than {113} facets in the growth process of α-Fe_2O_3 nanocrystals. Figure 4e shows a schematic illustration of supersaturation-controlled morphology evolution over reaction time. In general, the concentration of growth monomers gradually increases at the early stage of hydrolysis reaction. When the monomer concentration reaches a critical value at relatively high supersaturation, nucleation occurs, and subsequently the high supersaturation of the solution is gradually decreased to a relatively low value as the solute is consumed. The above supersaturation changes in the reaction contribute to the morphology evolution that α-Fe_2O_3 nanocrystals bound with facets of higher surface energy (e.g., {113}) are favored at the early stage of reaction, whereas the formed α-Fe_2O_3 nanocrystals are finally exposed with the stable facets of low energy (e.g., {012}).

In the syntheses of the bipyramid-Fe_2O_3-{113} and pseudocube-Fe_2O_3-{012} nanocrystals, the mixed solvent of ethanol and water was used as reaction medium. It is well-known that supersaturation is closely related to the solvent, in addition to the concentrations of precursors. Therefore, supersaturation-controlled morphology evolution of α-Fe_2O_3 nanocrystals can be likewise achieved by adjusting the ratio of water to ethanol in the reaction. Figure 5a shows that when the ratio of water to ethanol was 1:1, the products were pseudocubic Fe_2O_3 nanocrystals exposed with {012} facets. As the ratio of water to ethanol decreased to 1:10 (see Supporting Information, Table S3 for detailed conditions), some truncated pseudocubic nanocrystals enclosed with six

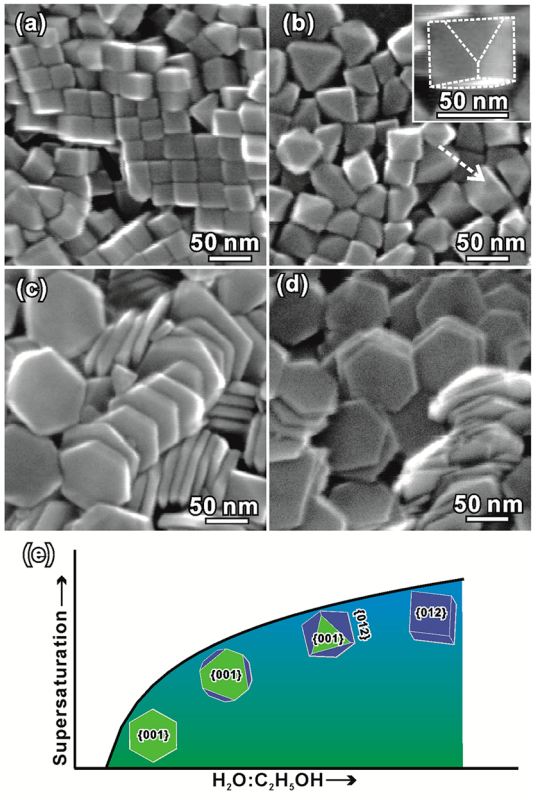

Figure 5. SEM images of α-Fe_2O_3 nanocrystals synthesized with different ratios of water to ethanol: (a) 1:1; (b) 1:10; (c) 3:100; (d) 1:100. (e) Schematic illustration of the supersaturation-controlled morphology evolution of α-Fe_2O_3 nanocrystals as a function of solubility in mixed solvents.

{012} and two {001} facets were produced together with pseudocubes, as shown in Figure 5b. (See Supporting Information, Figure S2 for detailed TEM characterization of truncated pseudocubes.) The lower ratio of water to ethanol led to a larger ratio of {001} to the total surface. When the ratio of water to ethanol decreased to 3:100 and 1:100, thick nanoplates (Figure 5c) and thin nanoplates (Figure 5d) were obtained, respectively. The thickness of thick nanoplates is ca. 20 nm, while the thickness of thin nanoplates is only less than 10 nm. Note that for the thin nanoplates, the side surfaces ({012}) are almost disregarded since the bottom/top surfaces ({001}) of thin nanoplates account for an overwhelming proportion of the exposed surface of nanoplates. It should be pointed out that as the ratio of water to ethanol was increased to 6:4 or 7:3, the as-obtained nanocrystals always presented a pseudocubic morphology, and their sizes ranged from 25 to 35 nm, which is slightly smaller than those obtained at the water to ethanol ratio of 1:1 (Supporting Information, Figure S3). When the ratio of H_2O to ethanol was further increased, the quantity of as-prepared Fe_2O_3 particles was reduced significantly. This is because the solubility of the precursor $Fe(acac)_3$ is very low in H_2O.

$Fe(acac)_3$ is slightly soluble in ethanol but insoluble in water. Therefore, the supersaturation of Fe^{3+} in solution increases as the content of water increases. That is to say, the supersaturation of Fe^{3+} is higher in the mixed solvent of higher water content (i.e., 1:1 and 1:10) than that of lower water content (i.e., 1:100 and 3:100). Previous calculation studies indicate that, for α-Fe_2O_3, the surface energy of {001} is lower than that of {012}, and accordingly {001} have the slower crystal growth rate.[44−46] Obviously, the morphology evolution from pseudocube-Fe_2O_3-{012} to plate-Fe_2O_3-{001}/{012} with the decrease of the water content in mixed solvent is consistent with the proposed supersaturation-controlled rule. This supersaturation-controlled morphology evolution as a function of the water/ethanol ratio is schematically illustrated in Figure 5e.

From the above concentration-, time-, and solvent-dependent experiments, it is concluded that the exposed facets of nanocrystals are thermodynamically determined by the supersaturation of growth monomers during crystal growth. The facets with high surface energy are favored in a high supersaturation solution, and stable facets with low surface energy are usually dominated in nanocrystals formed at equilibrium state with relatively low supersaturation solution.

3.3. Facet-Dependent Catalytic and Sensing Properties of α-Fe_2O_3 Nanocrystals. The surface structure, including exposed facets and their surface area, has been demonstrated to greatly affect the performance of materials in surface-related applications, typically catalysis and gas sensing. To investigate the surface effect on catalytic properties of α-Fe_2O_3, the catalytic oxidation of CO, which is very important to the practice of automotive exhaust catalysis and to the removal of CO from H_2-containing streams by preferential CO oxidation, was chosen as the probe reaction. The catalytic CO oxidation efficiency over the as-obtained bipyramid-Fe_2O_3-{113}, pseudocube-Fe_2O_3-{012}, and plate-Fe_2O_3-{001}/{012} nanocrystals was evaluated in a CO/air/N_2 stream, and all the samples were measured with the same mass (0.100 g). Usually, the more surface there is, the better the catalyst works. In our study, the BET-specific surface areas of the bipyramid-Fe_2O_3-{113}, pseudocube-Fe_2O_3-{012}, and plate-Fe_2O_3-{001}/{012} nanocrystals are measured to be 28.54, 29.66, 27.09 $m^2 \cdot g^{-1}$, respectively (see Supporting Information, Figure S4 for their nitrogen adsorption and desorption isotherms). Since the specific surface areas of the three samples are very close to each other, the influence of the surface areas between different samples can be negligible in comparing their catalytic properties.

Figure 6 shows the CO conversion curves over the three α-Fe_2O_3 samples as a function of temperature. The pseudocube-Fe_2O_3-{012} nanocrystals exhibits the best catalytic activity and reached 100% conversion at 280 °C. By contrast, the temperature of 100% conversion for the bipyramid-Fe_2O_3-{113} and plate-Fe_2O_3-{001}/{012} nanocrystals is higher, which is 300 and 360 °C, respectively. Furthermore, the

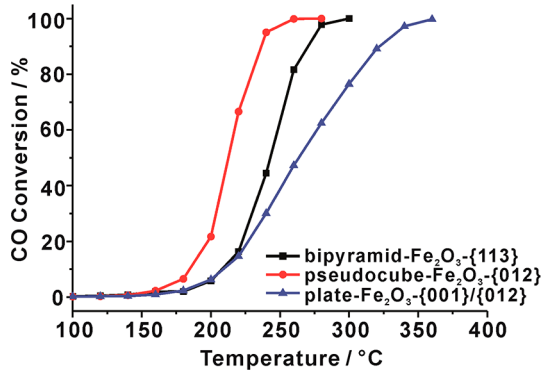

Figure 6. CO conversion curves of α-Fe_2O_3 nanocrystals with different shapes as a function of temperature.

dx.doi.org/10.1021/am502358g | ACS Appl. Mater. Interfaces 2014, 6, 12505−12514

starting conversion temperature over the pseudocube-Fe_2O_3-{012} nanocrystals is 160 °C, which is lower by 20 °C than that of the other two samples. This means that the {012} facets possess a lower activation barrier than the {113} and {001} facets for CO oxidation. From the above results, it can be deduced that for α-Fe_2O_3, the order of CO catalytic activity of the crystal facets is {012} > {113} > {001}.

As a common support for noble metal catalyst (such as Au, Pt, etc.), α-Fe_2O_3 has been intensively investigated in past years, with emphasis on the size effect toward the efficiency of CO oxidation reactions.[47,48] Recently, the influence from the exposed facets of bare α-Fe_2O_3 nanocrystals attracted increasing concerns. For example, the excellent catalytic performance of the pseudocubic α-Fe_2O_3 nanocrystals has been found in a previous study where the quasi-cubic nanocrystals with a low surface area unexpectedly exhibited a much higher activity in CO oxidation than the flowerlike nanostructure with higher surface area.[25,49] To explore the nature of facet-dependent catalytic activity in CO oxidation, CO chemisorption on the three samples was further measured. The results are shown in Table 2. Among the three samples, pseudocube-Fe_2O_3-{012}

Table 2. Chemisorption Amounts of CO on the Three α-Fe_2O_3 Catalysts

sample	chemisorption of CO (mL/g)
bipyramid-Fe_2O_3-{113}	0.186 ± 10
pseudocube-Fe_2O_3-{012}	0.254 ± 15
plate-Fe_2O_3-{001}/{012}	0.025 ± 5

nanocrystals showed the largest amount of chemisorbed CO, followed by bipyramid-Fe_2O_3-{113}, and plate-Fe_2O_3-{001}/{012} nanocrystals showed the lowest amount of chemisorbed CO. Obviously, such a result is coincident with the order of CO catalytic activity of the crystal facets, that is, {012} > {113} > {001}. CO chemisorption quantitatively reflects the amount of active sites on the surface of the blank nanocrystals. Therefore, the pseudocube-Fe_2O_3-{012} nanocrystals possess the most abundant active sites, thereby leading to the highest catalytic activity in CO oxidation.

Gas sensing is also one of the surface-related reaction procedures, which is essentially based on an abrupt response of surface or bulk resistance of metal oxide sensing materials when the ambient atmosphere changes. To the best of our knowledge, comprehensive investigation of gas-sensing properties of α-Fe_2O_3 nanocrystals has not been reported although some specific facets (such as {014}, {113}) were separately considered.[27,28,31] Here, we systematically investigated the gas-sensing properties of α-Fe_2O_3 nanocrystals enclosed by {113}, {012}, and {001}/{012} facets, respectively, using acetone and methanol as model analytes of volatile organic compounds (VOCs). Figure 7a shows sensing sensitivities of the three samples toward acetone of different concentrations at the operating temperature of 300 °C. Among them, the bipyramid-Fe_2O_3-{113} nanocrystals exhibited the best performance in acetone sensing, followed by pseudocube-Fe_2O_3-{012} and plate-Fe_2O_3-{001}/{012}. For example, under the given concentration of 200 ppm, the sensitivity of the three samples is 42.1 ± 5.7 (bipyramid-Fe_2O_3-{113}), 20.2 ± 3.5 (pseudocube-Fe_2O_3-{012}), and 6.2 ± 2.4 (plate-Fe_2O_3-{001}/{012}), respectively. The same facet-dependent sensing order was found in the sensing measurements of the three samples toward methanol (Figure 7b). It can be therefore

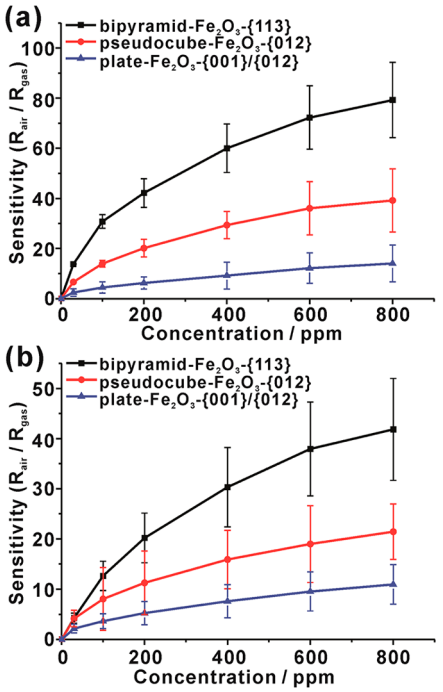

Figure 7. Concentration-dependent sensing curves of the α-Fe_2O_3 nanocrystals with different shapes: (a) acetone and (b) methanol.

concluded that the gas sensing properties of bare crystal surfaces are in the order of {113} > {012} > {001}.

For surface resistance-type metal oxide semiconductors like Fe_2O_3, the gas-sensing ability of facets is closely associated with their capacity of adsorbing oxygen, which greatly influences the thickness of the depletion layer near the surface of sensing materials. To verify the status of oxygen species adsorbed on the {113}, {012}, and {001} facets, X-ray photoelectron spectroscopy (XPS) analyses of the as-prepared three Fe_2O_3 samples (i.e., bipyramid-Fe_2O_3-{113}, pseudocube-Fe_2O_3-{012}, and plate-Fe_2O_3-{001}/{012}) were further carried out. Figure 8a shows Fe 2p XPS peaks of the three samples, in which the shakeup satellite line is characteristic of Fe^{3+} in

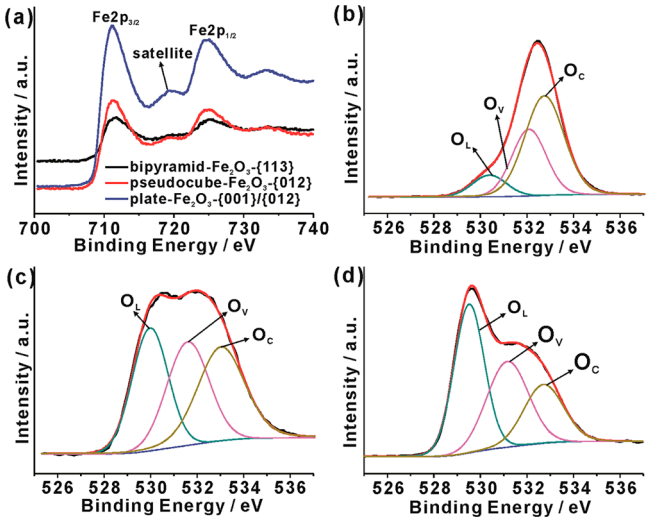

Figure 8. (a) Fe 2p XPS spectra and O 1s XPS spectra of the three samples: (b) bipyramid-Fe_2O_3-{113}, (c) pseudocube-Fe_2O_3-{012}, (d) plate-Fe_2O_3-{001}/{012}.

dx.doi.org/10.1021/am502358g | ACS Appl. Mater. Interfaces 2014, 6, 12505−12514

Fe_2O_3.[50] Figure 8b–d shows O 1s XPS peaks of each of the three samples, indicating that there are significant differences between oxygen states on the surface of three Fe_2O_3 samples. For the samples, the O 1s XPS peak can be decomposed into three fitted Gaussian components centered at ca. 530 eV (O_L), 531 (O_V), and 532 eV (O_C), respectively. The O_L component is attributed to O^{2-} ions in the Fe_2O_3 lattice, the O_V component at the medium binding energy is associated with O^{2-} ions in oxygen-deficient regions within the matrix of Fe_2O_3, and the O_C component is attributed to chemisorbed and dissociated oxygen species or OH.[51] Therefore, we can estimate the oxygen-chemisorbed ability of different exposed facets of Fe_2O_3 nanocrystal according to the intensity of O_C component in the O 1s XPS peak. As shown in Table 3, the percentages of

Table 3. Fitting Results of O 1s XPS Spectra of Three Fe_2O_3 Samples

sample	oxygen species	binding energy (eV)	relative percentage (%)
bipyramid-Fe_2O_3-{113}	O_L (Fe–O)	530.39	10.3
	O_V (vacancy)	532.09	32.8
	O_C (chemisorbed)	532.75	56.9
pseudocube-Fe_2O_3-{012}	O_L (Fe–O)	529.98	32.5
	O_V (vacancy)	531.60	32.1
	O_C (chemisorbed)	533.03	35.4
plate-Fe_2O_3-{001}/{012}	O_L (Fe–O)	529.51	43.3
	O_V (vacancy)	531.16	33.8
	O_C (chemisorbed)	532.71	22.9

both the O_V component and the O_C component follow the order of bipyramid-Fe_2O_3-{113} > pseudocube-Fe_2O_3-{012} > plate-Fe_2O_3-{001}/{012}, which is consistent with the order of the surface energy of their exposed facets. For three different samples, the relative percentages of the O_C component are about 56.85% (bipyramid-Fe_2O_3-{113}), 35.40% (pseudocube-Fe_2O_3-{012}), and 22.92% (plate-Fe_2O_3-{001}/{012}), respectively. These results reveal that the {113} facets of α-Fe_2O_3 are more active than the {012} and {001} facets for adsorption of ionized oxygen species. From the above analysis, it can be concluded that the extraordinary ability of chemisorbing oxygen of the bipyramid-Fe_2O_3-{113} nanocrystals greatly contributes to their high-performance gas sensing toward VOCs.

The facet-dependent gas sensing and catalytic properties of α-Fe_2O_3 nanocrystals are inherently associated with variation in the atomic configurations and chemical composition on different facets. Structurally, the crystal of α-Fe_2O_3 has a rhombohedrally centered hexagonal structure where Fe atoms in bulk are 6-fold coordinated with O atoms. However, the densities of Fe atoms and coordination environments on different planes, when they are exposed to the surface, are distinct. Supporting Information, Figure S5 displays surface atomic arrangements for the {113}, {012}, and {001} facets. For the {113} and {012} facets, Fe atoms are actually considered to be coordinatively unsaturated, because a large amount of dangling bonds are easily formed by losing original singly coordinated O atoms. Previous studies have demonstrated that compared to the {012} facets, the {113} facets display the lower density of low-coordination Fe atoms on the surface.[31,32,52,53] Interestingly, the {001} planes of α-Fe_2O_3 are referred to as repeating —Fe–O_3—Fe— atomic layers, and thus the {001} facets are actually terminated with either a single Fe or single O layer. For the Fe-terminated {001} facets, the density of low-coordination surface Fe atoms is 9.1 atoms·nm^{-2}. As the Fe- and O-terminated layers coexist on the {001} facets, the density of low-coordinated Fe atoms is actually halved, far smaller than that on {012} and {113} facets.[32,52] The low density of low-coordinated Fe atoms on the {001} facets would result in poor ability of adsorbing oxygen or other molecules, thereby leading to the worst performance of {001} faceted nanoplates in gas sensing and CO catalytic oxidation. It should be in particular stated that as surface reconstruction and/or solvation reaction occurs, the surface terminations (atomic structures and chemical compositions) under real environments are rather complicated. Therefore, it might be not enough that the facet-dependent properties of nanocrystals are explained merely by analysis on ideal crystal surfaces.

4. CONCLUSIONS

Through concentration-, reaction time- and solvent-dependent experiments under surfactant-free hydrothermal conditions, it was definitely demonstrated that the morphology evolution of the α-Fe_2O_3 nanocrystals was controlled by supersaturation of growth species in the reaction. The facets with high surface energy, such as {113}, tended to be formed in the reaction solution of high supersaturation, while the relatively more stable facets, such as {012} or {001}, were favored in the reaction solution of lower supersaturation. In addition, the catalytic activity of facets in CO oxidation was demonstrated to follow the order of {012} > {113} > {001}, while the sensing ability followed the order of {113} > {012} > {001}. The distinct catalytic and sensing performances of these specific faceted nanocrystals were ascribed to the deference of the adsorption capacity to CO and oxygen species, which is inherently determined by the density of Fe atoms and their coordination environments. Given the above, the present work will hopefully deepen our understanding of thermodynamics and kinetics control over the morphology of nanocrystals. More importantly, this work is a revelation to us that by engineering the surface structure, the performance of inorganic functional nanocrystals in surface-related applications can be significantly enhanced.

■ ASSOCIATED CONTENT

Supporting Information

Summary of detailed reaction parameters in concentration-, reaction time-, and solvent composition-dependent experiments, SEM and TEM characterizations of the products synthesized with different reaction times and solvents (Figures S1–3), the adsorption–desorption isotherms of samples (Figure S4), schematic illustration of surface terminations of α-Fe_2O_3 (Figure S5). This material is available free of charge via the Internet at http://pubs.acs.org.

■ AUTHOR INFORMATION

Corresponding Authors

*E-mail: qkuang@xmu.edu.cn. (Q.K.)
*E-mail: zxxie@xmu.edu.cn. (Z.X.)

Notes

The authors declare no competing financial interest.

■ ACKNOWLEDGMENTS

This work was supported by the National Basic Research Program of China (2011CBA00508 and 2013CB933901), the National Natural Science Foundation of China (21171142,

21131005, 21333008, and 21371144), and the program for New Century Excellent Talents in University (NCET-11-0294).

REFERENCES

(1) Tian, N.; Zhou, Z. Y.; Sun, S. G.; Ding, Y.; Wang, Z. L. Synthesis of Tetrahexahedral Platinum Nanocrystals with High-Index Facets and High Electro-Oxidation Activity. *Science* **2007**, *316*, 732−735.
(2) Han, X. G.; Jin, M. S.; Xie, S. F.; Kuang, Q.; Jiang, Z. Y.; Jiang, Y. Q.; Xie, Z. X.; Zheng, L. S. Synthesis of Tin Dioxide Octahedral Nanoparticles with Exposed High-Energy {221} Facets and Enhanced Gas-Sensing Properties. *Angew. Chem., Int. Ed.* **2009**, *48*, 9180−9183.
(3) Salant, A.; Shalom, M.; Tachan, Z.; Buhbut, S.; Zaban, A.; Banin, U. Quantum Rod-Sensitized Solar Cell: Nanocrystal Shape Effect on the Photovoltaic Properties. *Nano Lett.* **2012**, *12*, 2095−2100.
(4) Zhou, Z. Y.; Tian, N.; Li, J. T.; Broadwell, I.; Sun, S. G. Nanomaterials of High Surface Energy with Exceptional Properties in Catalysis and Energy Storage. *Chem. Soc. Rev.* **2011**, *40*, 4167−4185.
(5) Kuang, Q.; Wang, X.; Jiang, Z. Y.; Xie, Z. X.; Zheng, L. S. High-Energy-Surface Engineered Metal Oxide Micro- and Nanocrystallites and Their Applications. *Acc. Chem. Res.* **2014**, *47*, 308−318.
(6) Xia, Y. N.; Yang, P. D.; Sun, Y. G.; Wu, Y. Y.; Mayers, B.; Gates, B.; Yin, Y. D.; Kim, F.; Yan, Y. Q. One-Dimensional Nanostructures: Synthesis, Characterization, and Applications. *Adv. Mater.* **2003**, *15*, 353−389.
(7) Yang, H. G.; Sun, C. H.; Qiao, S. Z.; Zou, J.; Liu, G.; Smith, S. C.; Cheng, H. M.; Lu, G. Q. Anatase TiO_2 Single Crystals with A Large Percentage of Reactive Facets. *Nature* **2008**, *453*, 638−641.
(8) Sui, Y. M.; Fu, W. Y.; Yang, H. B.; Zeng, Y.; Zhang, Y. Y.; Zhao, Q.; Li, Y. E.; Zhou, X. M.; Leng, Y.; Li, M. H.; Zou, G. T. Low Temperature Synthesis of Cu_2O Crystals: Shape Evolution and Growth Mechanism. *Cryst. Growth Des.* **2010**, *10*, 99−108.
(9) Peng, Z.; Jiang, Y.; Song, Y.; Wang, C.; Zhang, H. Morphology Control of Nanoscale PbS Particles in a Polyol Process. *Chem. Mater.* **2008**, *20*, 3153−3162.
(10) Grimbergen, R. F. P.; Boek, E. S.; Meekes, H.; Bennema, P. Explanation for the Supersaturation Dependence of the Morphology of Lysozyme Crystals. *J. Cryst. Growth* **1999**, *207*, 112−121.
(11) Soare, L. C.; Bowen, P.; Lemaitre, J.; Hofmann, H. Precipitation of Nanostructured Copper Oxalate: Substructure and Growth Mechanism. *J. Phys. Chem. B* **2006**, *110*, 17763−17771.
(12) Kang, L. T.; Fu, H. B.; Cao, X. Q.; Shi, Q. A.; Yao, J. N. Controlled Morphogenesis of Organic Polyhedral Nanocrystals from Cubes, Cubooctahedrons, to Octahedrons by Manipulating the Growth Kinetics. *J. Am. Chem. Soc.* **2011**, *133*, 1895−1901.
(13) Lin, H. X.; Lei, Z. C.; Jiang, Z. Y.; Hou, C. P.; Liu, D. Y.; Xu, M. M.; Tian, Z. Q.; Xie, Z. X. Supersaturation-Dependent Surface Structure Evolution: From Ionic, Molecular to Metallic Micro/Nanocrystals. *J. Am. Chem. Soc.* **2013**, *135*, 9311−9314.
(14) Olson, T. Y.; Orme, C. A.; Han, T. Y. J.; Worsley, M. A.; Rose, K. A.; Satcher, J. H.; Kuntz, J. D. Shape Control Synthesis of Fluorapatite Structures Based on Supersaturation: Prismatic Nanowires, Ellipsoids, Star, and Aggregate Formation. *CrystEngComm* **2012**, *14*, 6384−6389.
(15) Li, S. W.; Xu, J. H.; Luo, G. S. Control of Crystal Morphology through Supersaturation Ratio and Mixing Conditions. *J. Cryst. Growth* **2007**, *304*, 219−224.
(16) Guo, H. B.; Barnard, A. S. Naturally Occurring Iron Oxide Nanoparticles: Morphology, Surface Chemistry, and Environmental Stability. *J. Mater. Chem. A* **2013**, *1*, 27−42.
(17) Guo, H. B.; Barnard, A. S. Modeling the Iron Oxides and Oxyhydroxides for the Prediction of Environmentally Sensitive Phase Transformations. *Phys. Rev. B* **2011**, *83*, 094112.
(18) Guo, H. B.; Xu, H. F.; Barnard, A. S. Can Hematite Nanoparticles Be an Environmental Indicator? *Energy Environ. Sci.* **2013**, *6*, 561−569.
(19) Wu, C. Z.; Yin, P.; Zhu, X.; OuYang, C. Z.; Xie, Y. Synthesis of Hematite (α-Fe_2O_3) Nanorods: Diameter Size and Shape Effects on Their Applications in Magnetism, Lithium Ion Battery, and Gas Sensors. *J. Phys. Chem. B* **2006**, *110*, 17806−17812.
(20) Fang, X. L.; Chen, C.; Jin, M. S.; Kuang, Q.; Xie, Z. X.; Xie, S. Y.; Huang, R. B.; Zheng, L. S. Single-Crystal-Like Hematite Colloidal Nanocrystal Clusters: Synthesis and Applications in Gas Sensors, Photocatalysis, and Water Treatment. *J. Mater. Chem.* **2009**, *19*, 6154−6160.
(21) Chen, J. S.; Zhu, T.; Yang, X. H.; Yang, H. G.; Lou, X. W. Top-Down Fabrication of α-Fe_2O_3 Single-Crystal Nanodiscs and Microparticles with Tunable Porosity for Largely Improved Lithium Storage Properties. *J. Am. Chem. Soc.* **2010**, *132*, 13162−13164.
(22) McDonald, K. J.; Choi, K. S. Photodeposition of Co-Based Oxygen Evolution Catalysts on α-Fe_2O_3 Photoanodes. *Chem. Mater.* **2011**, *23*, 1686−1693.
(23) Agarwala, S.; Lim, Z. H.; Nicholson, E.; Ho, G. W. Probing the Morphology-Device Relation of Fe_2O_3 Nanostructures Towards Photovoltaic and Sensing Applications. *Nanoscale* **2012**, *4*, 194−205.
(24) Lian, J. B.; Duan, X. C.; Ma, J. M.; Peng, P.; Kim, T. I.; Zheng, W. J. Hematite (α-Fe_2O_3) with Various Morphologies: Ionic Liquid-Assisted Synthesis, Formation Mechanism, and Properties. *ACS Nano* **2009**, *3*, 3749−3761.
(25) Zheng, Y. H.; Cheng, Y.; Wang, Y. S.; Bao, F.; Zhou, L. H.; Wei, X. F.; Zhang, Y. Y.; Zheng, Q. Quasicubic α-Fe_2O_3 Nanoparticles with Excellent Catalytic Performance. *J. Phys. Chem. B* **2006**, *110*, 3093−3097.
(26) He, S.; Wang, G. S.; Wang, J. W.; Wei, Y. Z.; Wu, Y.; Guo, L.; Cao, M. S. Facile Size-Controllable Synthesis of Colorful Quasi-Cubic α-Fe_2O_3 Materials from Nanoscale to Microscale and Their Properties Related to the Size Effect. *ChemPlusChem* **2013**, *78*, 875−883.
(27) Liu, X. H.; Zhang, J.; Wu, S. H.; Yang, D. J.; Liu, P. R.; Zhang, H. M.; Wang, S. R.; Yao, X. D.; Zhu, G. S.; Zhao, H. J. Single Crystal α-Fe_2O_3 with Exposed {104} Facets for High-Performance Gas-Sensor Applications. *RSC Adv.* **2012**, *2*, 6178−6184.
(28) Li, X. L.; Wei, W. J.; Wang, S. Z.; Kuai, L.; Geng, B. Y. Single-Crystalline α-Fe_2O_3 Oblique Nanoparallelepipeds: High-Yield Synthesis, Growth Mechanism, and Structure Enhanced Gas-Sensing Properties. *Nanoscale* **2011**, *3*, 718−724.
(29) Chatman, S.; Zarzycki, P.; Preoanin, T.; Rosso, K. M. Effect of Surface Site Interactions on Potentiometric Titration of Hematite (α-Fe_2O_3) Crystal Faces. *J. Colloid Interface Sci.* **2013**, *391*, 125−134.
(30) Van, T. K.; Cha, H. G.; Nguyen, C. K.; Kim, S. W.; Jung, M. H.; Kang, Y. S. Nanocystals of Hematite with Unconventional Shape-Truncated Hexagonal Bipyramid and Its Optical and Magnetic Properties. *Cryst. Growth Des.* **2012**, *12*, 862−868.
(31) Yang, Y.; Ma, H. X.; Zhuang, J.; Wang, X. Morphology-Controlled Synthesis of Hematite Nanocrystals and Their Facet Effects on Gas-Sensing Properties. *Inorg. Chem.* **2011**, *50*, 10143−10151.
(32) Zhou, X. M.; Lan, J. Y.; Liu, G.; Deng, K.; Yang, Y. L.; Nie, G. J.; Yu, J. G.; Zhi, L. J. Facet-Mediated Photodegradation of Organic Dye over Hematite Architectures by Visible Light. *Angew. Chem., Int. Ed.* **2012**, *51*, 178−182.
(33) Xu, W. H.; Meng, Q. Q.; Gao, C.; Wang, J.; Li, Q. X.; Liu, J. H.; Huang, X. J. Investigation of the Facet-Dependent Performance of α-Fe_2O_3 Nanocrystals for Heavy Metal Determination by Stripping Voltammetry. *Chem. Commun.* **2014**, *50*, 5011−5013.
(34) Lin, M.; Tan, H. R.; Tan, J. P. Y.; Bai, S. Q. Understanding the Growth Mechanism of α-Fe_2O_3 Nanoparticles through a Controlled Shape Transformation. *J. Phys. Chem. C* **2013**, *117*, 11242−11250.
(35) Rodriguez, R. D.; Demaille, D.; Lacaze, E.; Jupille, J.; Chaneac, C.; Jolivet, J. P. Rhombohedral Shape of Hematite Nanocrystals Synthesized via Thermolysis of an Additive-Free Ferric Chloride Solution. *J. Phys. Chem. C* **2007**, *111*, 16866−16870.
(36) Gao, F.; Liu, R. M.; Yin, J. Z.; Lu, Q. Y. Synthesis of Polyhedral Iron Oxide Nanocrystals Bound by High-Index Facets. *Sci. China: Chem.* **2014**, *57*, 114−121.
(37) Liu, R. M.; Jiang, Y. W.; Fan, H.; Lu, Q. Y.; Du, W.; Gao, F. Metal Ions Induce Growth and Magnetism Alternation of α-Fe_2O_3

Crystals Bound by High-Index Facets. *Chem.—Eur. J.* **2012**, *18*, 8957−8963.
(38) Yin, J. Z.; Yu, Z. N.; Gao, F.; Wang, J. J.; Pang, H. A.; Lu, Q. Y. Low-Symmetry Iron Oxide Nanocrystals Bound by High-Index Facets. *Angew. Chem., Int. Ed.* **2010**, *49*, 6328−6332.
(39) Han, X.-G.; He, H.-Z.; Kuang, Q.; Zhou, X.; Zhang, X.-H.; Xu, T.; Xie, Z.-X.; Zheng, L.-S. Controlling Morphologies and Tuning the Related Properties of Nano/Microstructured ZnO Crystallites. *J. Phys.Chem. C* **2009**, *113*, 584−589.
(40) Chen, L. Q.; Yang, X. F.; Chen, J. A.; Liu, J.; Wu, H.; Zhan, H. Q.; Liang, C. L.; Wu, M. M. Continuous Shape- and Spectroscopy-Tuning of Hematite Nanocrystals. *Inorg. Chem.* **2010**, *49*, 8411−8420.
(41) Murray, C. B.; Kagan, C. R.; Bawendi, M. G. Synthesis and Characterization of Monodisperse Nanocrystals and Close-Packed Nanocrystal Assemblies. *Annu. Rev. Mater. Sci.* **2000**, *30*, 545−610.
(42) Markov, I. V. *Crystal Growth for Beginners: Fundamentals of Nucleation, Crystal Growth and Epitaxy,* 2nd ed.; World Scientific: Singapore, 2003.
(43) Demianets, L. N.; Pouchko, S. V.; Gaynutdinov, R. V. Fe_2O_3 Single Crystals: Hydrothermal Growth, Crystal Chemistry and Growth Morphology. *J. Cryst. Growth* **2003**, *259*, 165−178.
(44) Guo, H. B.; Barnard, A. Thermodynamic Modeling of Nanomorphologies of Hematite and Goethite. *J. Mater. Chem.* **2011**, *21*, 11566−11577.
(45) Guo, H. B.; Barnard, A. S. Environmentally Dependent Stability of Low-Index Hematite Surface. *J. Colloid Interface Sci.* **2012**, *386*, 315−324.
(46) Reeves, N. J.; Mann, S. Influence of Inorganic and Organic Additives on the Tailored Synthesis of Iron Oxides. *J. Chem. Soc., Faraday Trans.* **1991**, *87*, 3875−3880.
(47) Sonström, P.; Arndt, D.; Wang, X.; Zielasek, V.; Bäumer, M. Ligand Capping of Colloidally Synthesized Nanoparticles—A Way to Tune Metal-Support Interactions in Heterogeneous Gas-Phase Catalysis. *Angew. Chem., Int. Ed.* **2011**, *50*, 3888−3891.
(48) Guo, X.; Fu, Q.; Ning, Y.; Wei, M.; Li, M.; Zhang, S.; Jiang, Z.; Bao, X. Ferrous Centers Confined on Core−Shell Nanostructures for Low-Temperature CO Oxidation. *J. Am. Chem. Soc.* **2012**, *134*, 12350−12353.
(49) Mou, X. L.; Wei, X. J.; Li, Y.; Shen, W. J. Tuning Crystal-Phase and Shape of Fe_2O_3 Nanoparticles for Catalytic Applications. *CrystEngComm* **2012**, *14*, 5107−5120.
(50) Gao, Y.; Chambers, S. A. Heteroepitaxial Growth of α-Fe_2O_3, γ-Fe_2O_3, and Fe_3O_4 Thin Films by Oxygen-Plasma-Assisted Molecular Beam Epitaxy. *J. Cryst. Growth* **1997**, *174*, 446−451.
(51) Dupin, J.-C.; Gonbeau, D.; Vinatier, P.; Levasseur, A. Systematic XPS Studies of Metal Oxides, Hydroxides, and Peroxides. *Phys. Chem. Chem. Phys.* **2000**, *2*, 1319−1324.
(52) Lv, B. L.; Liu, Z. Y.; Tian, H.; Xu, Y.; Wu, D.; Sun, Y. H. Single-Crystalline Dodecahedral and Octodecahedral α-Fe_2O_3 Particles Synthesized by a Fluoride Anion−Assisted Hydrothermal Method. *Adv. Funct. Mater.* **2010**, *20*, 3987−3996.
(53) Chatman, S.; Zarzycki, P.; Rosso, K. M. Surface Potentials of (001), (012), (113) Hematite (α-Fe_2O_3) Crystal Faces in Aqueous Solution. *Phys. Chem. Chem. Phys.* **2013**, *15*, 13911−13921.